

Two-Dimensional Covalent Organic Frameworks for Carbon Dioxide Capture through Channel-Wall Functionalization

Ning Huang, Xiong Chen, Rajamani Krishna, and Donglin Jiang*

Abstract: Ordered open channels found in two-dimensional covalent organic frameworks (2D COFs) could enable them to adsorb carbon dioxide. However, the frameworks' dense layer architecture results in low porosity that has thus far restricted their potential for carbon dioxide adsorption. Here we report a strategy for converting a conventional 2D COF into an outstanding platform for carbon dioxide capture through channel-wall functionalization. The dense layer structure enables the dense integration of functional groups on the channel walls, creating a new version of COFs with high capacity, reusability, selectivity, and separation productivity for flue gas. These results suggest that channel-wall functional engineering could be a facile and powerful strategy to develop 2D COFs for high-performance gas storage and separation.

Covalent organic frameworks (COFs), a class of crystalline porous polymers that allow the atomically precise integration of building blocks into periodicities, have emerged as a new platform for designing advanced organic materials with periodic structures.^[1–5] Two-dimensional (2D) COFs have limited surface areas and small pore volumes as a result of their dense π -stacking layer structure, which greatly restricts their potential as a porous medium for the adsorption of gases such as carbon dioxide, methane, and hydrogen. With the exception of two examples utilizing azine^[2b] and boronate^[3d] linkages that interact with specific gas molecules to exhibit good capacity, the majority of 2D COFs have very low performance in gas adsorption. To improve this situation, we present a strategy that explores the channel walls for functional engineering and demonstrate its significance and effectiveness in the design of 2D COFs for high-performance gas adsorption and separation.

The advantage of the dense layer structure of 2D COFs is that this architecture enables the dense incorporation of functional groups onto the channel walls. This structural benefit compensates for the low porosity of 2D COFs. We observed that functional engineering of the channel walls converts a conventional 2D COF into an outstanding carbon-dioxide-capture material. We demonstrated this strategy by using a conventional imine-linked 2D COF (Figure 1 a,b, [HO]_{100%}-H₂P-COF) as a scaffold with porphyrin at the vertices and phenol units on the pore walls; this 2D COF exhibits a low capacity for carbon dioxide adsorption. The phenol groups undergo a quantitative ring opening reaction with succinic anhydride that decorates the channel walls with open carboxylic acid groups (Figure 1 a,c, [HO₂C]_{100%}-H₂P-COF). The content of carboxylic acid units on the channel walls was tuned by adjusting the content of phenol groups through a three-component condensation system with a mixture of 2,5-dihydroxyterephthalaldehyde (DHTA) and 1,4-phthalaldehyde (PA) as the wall components (Figure 1 a, [HO]_{X%}-H₂P-COFs, $X = [\text{DHTA}]/([\text{DHTA}] + [\text{PA}])$). Various analytic methods revealed that the DHTA-to-PA molar ratios integrated into [HO]_{X%}-H₂P-COFs were identical to those employed for the reactions (see the Supporting Information, SI, Table S1, Figures S1 and S2). Using this method, we synthesized a series of [HO₂C]_{X%}-H₂P-COFs with controlled carboxylic acid density that varied from 25% to 50%, 75%, and 100% (Figure 1 a). The [HO₂C]_{X%}-H₂P-COFs were characterized by using infrared spectroscopy (Figure S1), elemental and thermogravimetric analysis (Table S1, Figure S3), energy dispersive X-ray spectroscopy (Table S2, Figure S4), solution-state ¹H NMR spectroscopy of hydrolyzed samples (Table S3, Figure S5), and X-ray diffraction (XRD) measurements. These methods show that the content of carboxylic acid units integrated into the channel walls is close to the X% value of [HO₂C]_{X%}-H₂P-COFs (Table S3). Notably, compared to metal-catalyzed azide-ethynyl^[2c,d] or other click reactions,^[4c] this ring opening reaction is free of metal catalysts, proceeds smoothly and cleanly, and excludes the formation of metal nanoparticles that would contaminate the channels.

The [HO]_{100%}-H₂P-COF samples exhibited strong XRD peaks at 3.49°, 7.21°, and 23.1°, which are assignable to 100, 200, and 001 facets, respectively (Figure 1 d, red curve).^[2d] Other [HO]_{X%}-H₂P-COFs exhibited identical diffraction patterns (Figure 1 d). The [HO₂C]_{X%}-H₂P-COFs exhibit XRD patterns (Figure 1 e) similar to those of [HO]_{X%}-H₂P-COFs, which indicates that the crystal structure of [HO₂C]_{X%}-H₂P-COFs is similar to that of [HO]_{100%}-H₂P-COF.^[2d] The presence of (001) facet at 23.1°, which corresponds to an interlayer interval of 3.8 Å, indicates that [HO]_{X%}-H₂P-COFs

[*] N. Huang, Dr. X. Chen, Prof. Dr. D. Jiang
Department of Materials Molecular Science
Institute for Molecular Science
National Institutes of Natural Sciences
5-1 Higashiyama, Myodaiji, Okazaki 444-8787 (Japan)
E-mail: jiang@ims.ac.jp
Prof. Dr. R. Krishna
Van't Hoff Institute for Molecular Sciences
University of Amsterdam
Science Park 904, 1098 XH Amsterdam (The Netherlands)

Supporting information for this article is available on the WWW under <http://dx.doi.org/10.1002/anie.201411262>.

© 2015 The Authors. Published by Wiley-VCH Verlag GmbH & Co. KGaA. This is an open access article under the terms of the Creative Commons Attribution Non-Commercial License, which permits use, distribution and reproduction in any medium, provided the original work is properly cited and is not used for commercial purposes.

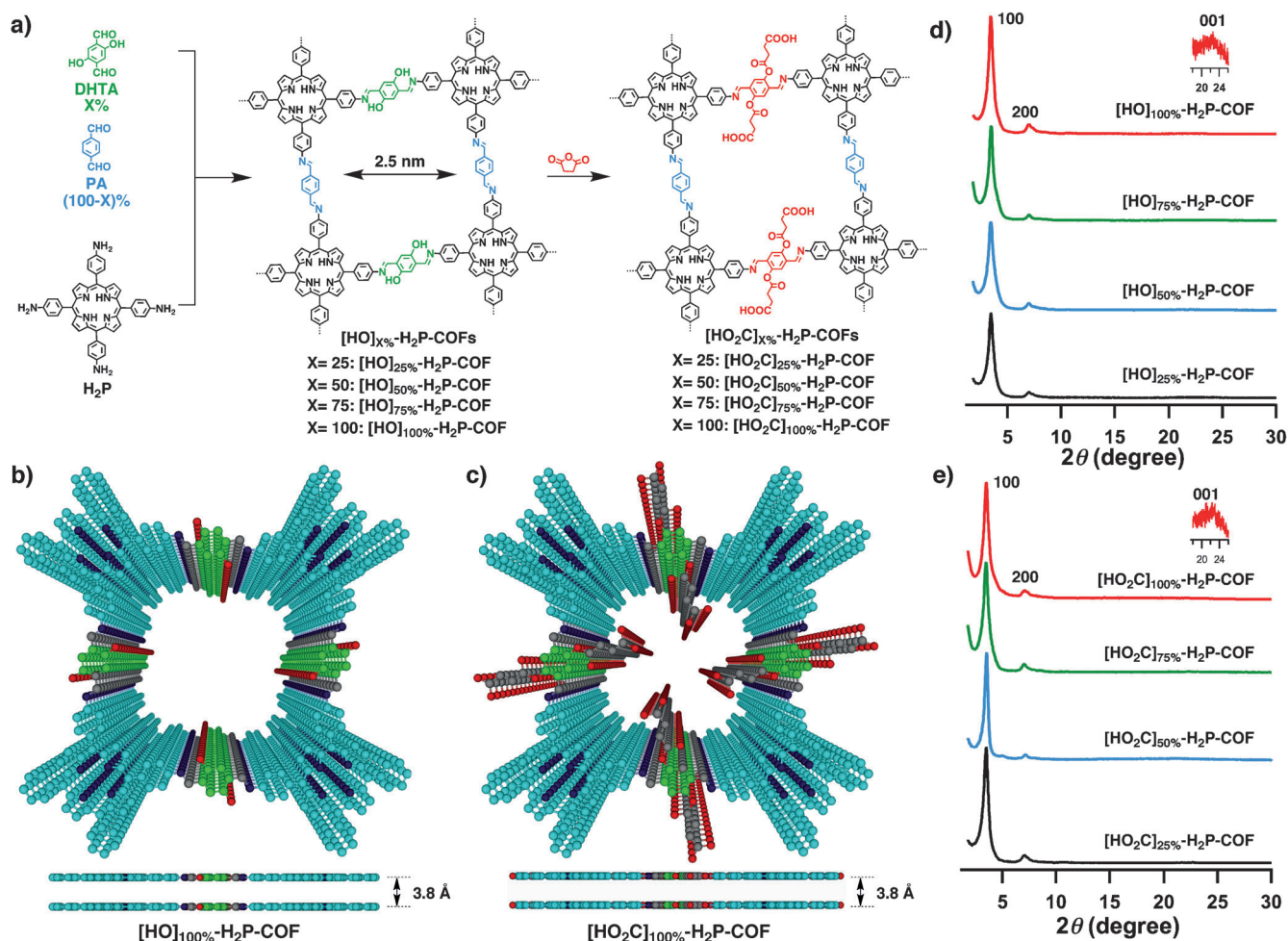


Figure 1. a) Synthesis of $[\text{HO}_2\text{C}]_X\text{-H}_2\text{P-COFs}$ with channel walls functionalized with carboxylic acid groups through the ring opening reaction of $[\text{HO}]_X\text{-H}_2\text{P-COFs}$ with succinic anhydride. Top views of b) $[\text{HO}]_{100\%}\text{-H}_2\text{P-COF}$ and c) $[\text{HO}_2\text{C}]_{100\%}\text{-H}_2\text{P-COF}$. XRD patterns of d) $[\text{HO}]_X\text{-H}_2\text{P-COFs}$ and e) $[\text{HO}_2\text{C}]_X\text{-H}_2\text{P-COFs}$.

and $[\text{HO}_2\text{C}]_X\text{-H}_2\text{P-COFs}$ have dense π -stacking layer structures (Figure 1 b,c).

The crystal structures of $[\text{HO}]_X\text{-H}_2\text{P-COFs}$ and $[\text{HO}_2\text{C}]_X\text{-H}_2\text{P-COFs}$ suggest the presence of open nano-channels (Figure 1 b,c). The $[\text{HO}]_X\text{-H}_2\text{P-COFs}$ exhibit typical type IV nitrogen sorption isotherm profiles indicative of mesoporous character (Figure S6a). Notably, the Brunauer–Emmett–Teller (BET) surface area ($1054\text{--}1284\text{ m}^2\text{ g}^{-1}$), pore volume ($0.89\text{--}1.02\text{ cm}^3\text{ g}^{-1}$), and pore size (2.5 nm) remained nearly unchanged (Table 1). Pore size distribution profiles revealed that these COFs possess a single type of mesopores (Figure S6b–e). Therefore, the three-component condensation reaction is reasonably concluded to allow for the integration of phenol groups in a controlled manner while retaining crystallinity and porosity.

Functionalization of the channel walls with carboxylic acid groups triggers microporosity in $[\text{HO}_2\text{C}]_X\text{-H}_2\text{P-COFs}$, as evidenced by their typical type I sorption curves (Figure S6f). The BET surface area (S_{BET}) decreased from 786 to 673 , 482 , and $364\text{ m}^2\text{ g}^{-1}$, whereas the pore size decreased from 2.2 to 1.9 , 1.7 , and 1.4 nm (Table 1), as the content of carboxylic groups was increased from 25% to 50% , 75% , and

100% , respectively. The pore volume also decreased from 0.78 to 0.66 , 0.54 , and $0.43\text{ cm}^3\text{ g}^{-1}$, as the content of carboxylic groups was increased. This reduction in porosity is indicative of space filling by the functional units appended to the channel walls. Notably, the pore size distribution profiles revealed that porosity was solely derived from the micropores (Figure S6g–j). This observation also suggests that the chan-

Table 1: Porosity, CO_2 uptake, and Q_{st} value of $[\text{HO}]_X\text{-H}_2\text{P-COFs}$ and $[\text{HO}_2\text{C}]_X\text{-H}_2\text{P-COFs}$.

$\text{H}_2\text{P-COFs}$	S_{BET} [$\text{m}^2\text{ g}^{-1}$]	Pore size [nm]	Pore volume [$\text{cm}^3\text{ g}^{-1}$]	CO_2 uptake [mg g^{-1}] at 1 bar 273 K	Q_{st} [kJ mol^{-1}] 298 K	
$[\text{HO}]_{25\%}$	1054	2.5	0.89	54	31	32.2
$[\text{HO}]_{50\%}$	1089	2.5	0.91	46	34	29.4
$[\text{HO}]_{75\%}$	1153	2.5	0.96	52	32	31.5
$[\text{HO}]_{100\%}$	1284	2.5	1.02	63	35	36.4
$[\text{HO}_2\text{C}]_{25\%}$	786	2.2	0.78	96	58	38.2
$[\text{HO}_2\text{C}]_{50\%}$	673	1.9	0.66	134	67	39.6
$[\text{HO}_2\text{C}]_{75\%}$	482	1.7	0.54	157	72	41.2
$[\text{HO}_2\text{C}]_{100\%}$	364	1.4	0.43	174	76	43.5

nel walls were randomly functionalized with carboxylic acid groups in the case of $[\text{HO}_2\text{C}]_X\text{-H}_2\text{P-COFs}$ ($X=25, 50,$ and 75). Stability tests showed that $[\text{HO}_2\text{C}]_X\text{-H}_2\text{P-COF}$ was stable upon immersion in THF, water, and aqueous HCl (1M), NaHCO_3 (1M), and KOH (1M) solutions for 24 h (Figure S7).

Carboxylic acid groups have been reported to trigger a dipolar interaction with carbon dioxide.^[6a-f] In $[\text{HO}_2\text{C}]_X\text{-H}_2\text{P-COFs}$, the carboxylic acid units are located at the termini and exhibit an acidity similar to that of the free carboxylic acid, as evidenced by their $\text{p}K_a$ value of 5.86. We first investigated the CO_2 adsorption by $[\text{HO}]_X\text{-H}_2\text{P-COFs}$ at pressures up to 1 bar and at temperatures of 273 K (Figure S8a) and 298 K (Figure S8b). The $[\text{HO}]_X\text{-H}_2\text{P-COFs}$ exhibited low capacities between 46 and 63 mg g^{-1} at 273 K and between 31 and 35 mg g^{-1} at 298 K (Table 1). By contrast, the $[\text{HO}_2\text{C}]_X\text{-H}_2\text{P-COFs}$ exhibited dramatically increased CO_2 adsorption capacities. For example, $[\text{HO}_2\text{C}]_{100}\text{-H}_2\text{P-COF}$ exhibited a capacity of 180 and 76 mg g^{-1} at 273 K (Figure S8c) and 298 K (Figure S8d), respectively. These capacities are 2.8- and 2.2-fold greater than those of $[\text{HO}]_{100}\text{-H}_2\text{P-COF}$ (Table 1). Interestingly, the adsorption capacity of $[\text{HO}_2\text{C}]_X\text{-H}_2\text{P-COFs}$ increased in proportion to their carboxylic acid content (Figure S8c,d; Table 1). These positive effects clearly confirmed the effectiveness of channel-wall functionalization in enhancing CO_2 adsorption.

Various 2D and 3D COFs with different structures have been previously synthesized and investigated in attempts to develop a practical scaffold for carbon dioxide adsorption. Typical examples include boronate-linked 2D COF-5 (5.9 wt %, $S_{\text{BET}} = 1670 \text{ m}^2 \text{ g}^{-1}$),^[3c] TDCOF-5 (9.2 wt %, $S_{\text{BET}} = 2497 \text{ m}^2 \text{ g}^{-1}$),^[5a] and 3D COF-103 (7.6 wt %, $S_{\text{BET}} = 3530 \text{ m}^2 \text{ g}^{-1}$),^[3e] imine-linked ILCOF-1 (6.0 wt %, $S_{\text{BET}} = 2723 \text{ m}^2 \text{ g}^{-1}$)^[5b] and TpPa-1 (15.6 wt %, $S_{\text{BET}} = 535 \text{ m}^2 \text{ g}^{-1}$),^[3d] and azine-linked ACOF-1 (17.7 wt %, $S_{\text{BET}} = 1176 \text{ m}^2 \text{ g}^{-1}$).^[2b] The capacity of $[\text{HO}]_{100}\text{-H}_2\text{P-COF}$ (6.5 wt %) is close to those of conventional and nonfunctionalized COF-5, ILCOF-1, and COF-103. By contrast, the wall-channel functionalized $[\text{HO}_2\text{C}]_{100}\text{-H}_2\text{P-COF}$ takes up 4.1 mmol g^{-1} of CO_2 (18.0 wt %, 180 mg g^{-1} , $S_{\text{BET}} = 364 \text{ m}^2 \text{ g}^{-1}$), which is the highest performance among 2D and 3D COFs reported thus far. To the best of our knowledge, the capacity observed for $[\text{HO}_2\text{C}]_{100}\text{-H}_2\text{P-COF}$ is also comparable to those of other top-class members (Table S1), including PPN-6- SO_3Li (187 mg g^{-1}),^[6g] Amine-PCN-58 (128 mg g^{-1}),^[6p] UCBZ-1 (99 mg g^{-1}),^[6q] N-TC-EMC (176 mg g^{-1}),^[6 h] and PPN-6- CH_2DETA (190 mg g^{-1}).^[6i]

Upon functionalization with carboxylic acid groups that have affinity for carbon dioxide, $[\text{HO}_2\text{C}]_{100}\text{-H}_2\text{P-COF}$ may exhibit enhanced adsorption selectivity. Based on the CO_2 and N_2 sorption isotherm curves measured at 298 K (Figures S8 and S9), we investigated the selective adsorption of CO_2 over N_2 , which is critical for carbon capture from air or flue gas streams. The ideal adsorbed solution theory (IAST) of Myers and Prausnitz^[7a] is a well-established model for describing the adsorption of gas mixtures in porous materials. Using pure-component isotherm fits, we determined the adsorption selectivity defined by $S_{\text{ads}} = (q_1/q_2)/(p_1/p_2)$ using the IAST method (SI). The accuracy of the IAST calculations for estimating the component loadings for several binary

mixtures in a wide variety of porous materials has been established by comparison with configurational-bias Monte Carlo (CBMC) simulations of mixture adsorption. We utilized $[\text{HO}]_{100}\text{-H}_2\text{P-COF}$ and $[\text{HO}_2\text{C}]_{100}\text{-H}_2\text{P-COF}$ for the separation of a CO_2/N_2 mixture that is relevant for CO_2 capture from flue gases and for our evaluation we assumed the CO_2/N_2 mixtures contained 15% CO_2 and 85% N_2 , following the earlier work of Mason et al.^[6l] Figure 2a and b show the IAST calculation of CO_2 and N_2 uptake capacities for the 15/85 CO_2/N_2 mixture at 298 K. Notably, $[\text{HO}_2\text{C}]_{100}\text{-H}_2\text{P-COF}$ exhib-

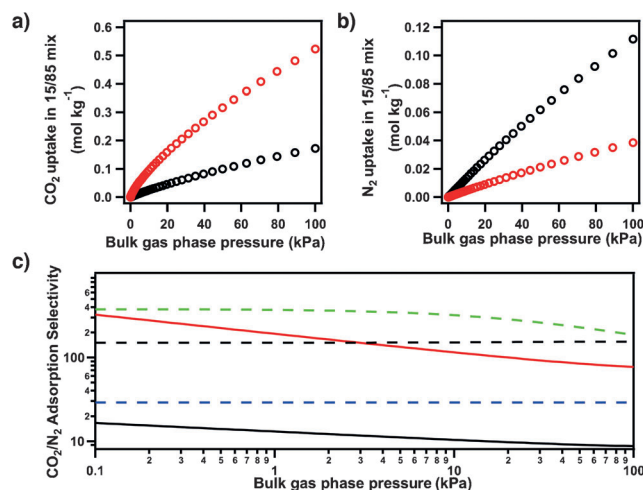


Figure 2. a) CO_2 and b) N_2 uptake by $[\text{HO}]_{100}\text{-H}_2\text{P-COF}$ (black circles) and $[\text{HO}_2\text{C}]_{100}\text{-H}_2\text{P-COF}$ (red circles) of a 15/85 CO_2/N_2 flue gas mixture at 298 K. c) CO_2/N_2 adsorption selectivity of $[\text{HO}]_{100}\text{-H}_2\text{P-COF}$ (black curve) and $[\text{HO}_2\text{C}]_{100}\text{-H}_2\text{P-COF}$ (red curve) for the 15/85 CO_2/N_2 flue gas mixture at 298 K. The selectivities of NaX zeolite (broken blue curve), CuBTC (broken black curve), and MgMOF-74 (broken green curve) are shown for comparison.

ited a CO_2 uptake capacity of 0.51 mol kg^{-1} at 100 kPa (= 1 bar), whereas $[\text{HO}]_{100}\text{-H}_2\text{P-COF}$ displayed an uptake of only 0.16 mol kg^{-1} (Figure 2a). By contrast, $[\text{HO}]_{100}\text{-H}_2\text{P-COF}$ exhibited an N_2 uptake of 0.118 mol kg^{-1} , which is substantially greater than that of $[\text{HO}_2\text{C}]_{100}\text{-H}_2\text{P-COF}$ (0.038 mol kg^{-1} , Figure 2b). These results clearly suggest that the functionalization of channel walls with carboxylic acid groups significantly enhances the CO_2 adsorption capacity of the flue mixture gas. Figure 3c presents the adsorption selectivity for the 15/85 CO_2/N_2 flue gas mixture, in comparison to those of CuBTC (a MOF),^[6j] MgMOF-74,^[6k-n] and NaX zeolite.^[6n,o] At low pressures, such as 0.1 kPa, the adsorption selectivity S_{ads} was 323, which is greater than that of both CuBTC (broken black curve) and NaX zeolite (broken blue curve) and is close to that of MgMOF-74 (broken green curve). By contrast, $[\text{HO}]_{100}\text{-H}_2\text{P-COF}$ exhibited a selectivity of only 18 at 0.1 kPa. At 100 kPa, $[\text{HO}_2\text{C}]_{100}\text{-H}_2\text{P-COF}$ exhibited a selectivity of 77, whereas $[\text{HO}]_{100}\text{-H}_2\text{P-COF}$ exhibited a selectivity of only 8. Notably, the selectivity of $[\text{HO}_2\text{C}]_{100}\text{-H}_2\text{P-COF}$ is sufficiently high for potential practical use.

To clarify the nature of CO_2 adsorption, the isosteric heat of adsorption (Q_{st}) was calculated from the CO_2 adsorption

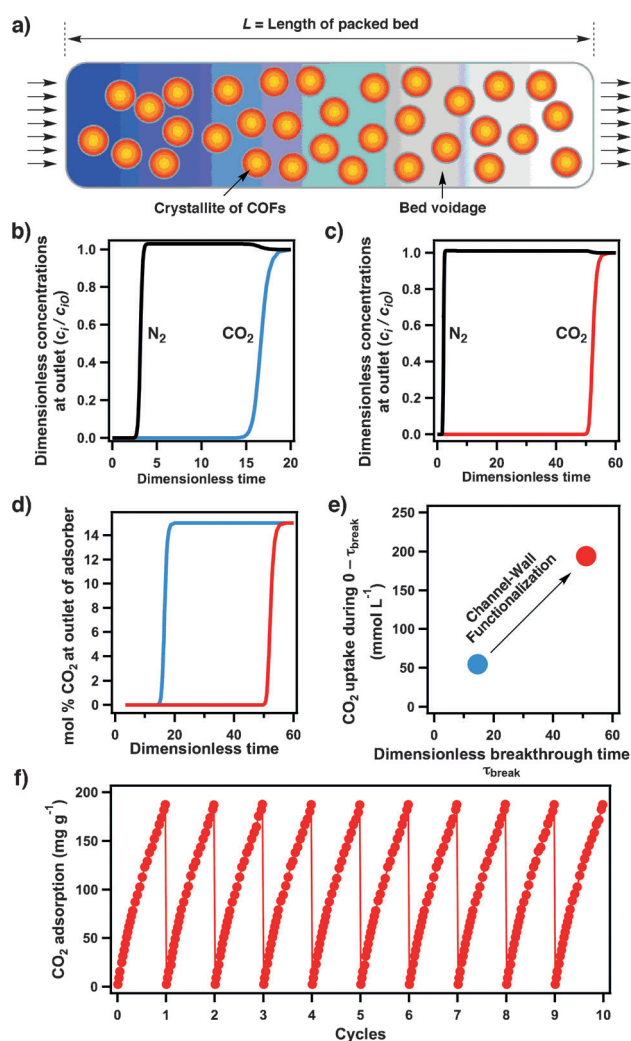


Figure 3. a) Fixed-bed adsorber for COFs. Flue gas breakthrough profiles of b) $[\text{HO}]_{100\%}\text{-H}_2\text{P-COF}$ and c) $[\text{HO}_2\text{C}]_{100\%}\text{-H}_2\text{P-COF}$ at 298 K. d) Comparison of % CO_2 at the adsorber outlet at 298 K (blue curve: $[\text{HO}]_{100\%}\text{-H}_2\text{P-COF}$, red curve: $[\text{HO}_2\text{C}]_{100\%}\text{-H}_2\text{P-COF}$). e) Comparison of CO_2 capture productivity at 298 K (blue spot: $[\text{HO}]_{100\%}\text{-H}_2\text{P-COF}$, red spot: $[\text{HO}_2\text{C}]_{100\%}\text{-H}_2\text{P-COF}$). f) Cycle test of $[\text{HO}_2\text{C}]_{100\%}\text{-H}_2\text{P-COF}$ at 273 K.

isotherms measured at pressures up to 1 bar and at temperatures at 273 and 298 K. Interestingly, the Q_{st} value increased proportionally with the carboxylic acid content (Table 1). Therefore, the functionalized walls facilitate interactions with CO_2 and contribute to the enhanced performance. The Q_{st} value was 43.5 kJ mol^{-1} for $[\text{HO}_2\text{C}]_{100\%}\text{-H}_2\text{P-COF}$, which is compatible to that for MgMOF-74 and much higher than those for $[\text{HO}]_{100\%}\text{-H}_2\text{P-COF}$ (34.5 kJ mol^{-1}), CuBTC , and NaX zeolite.

To evaluate the gas separation ability of adsorbents under kinetic flowing gas conditions, breakthrough simulations were performed using a precise methodology established by Krishna and Long (SI).^[7b] These simulations properly reflect the separation capability of a pressure-swing adsorption (PAS) process, which is an energetically efficient method for industrial-scale capture. The performance of a COF in a PSA unit is governed by both selectivity and capacity factors.

Figure 3a presents a schematic of a packed-bed adsorber. Figure 3b and c show typical breakthrough curves for $[\text{HO}]_{100\%}\text{-H}_2\text{P-COF}$ and $[\text{HO}_2\text{C}]_{100\%}\text{-H}_2\text{P-COF}$, respectively. The x -axis is dimensionless time, τ , defined as dividing the actual time, t , by the characteristic time, L/μ (SI). Clearly, $[\text{HO}_2\text{C}]_{100\%}\text{-H}_2\text{P-COF}$ exhibited a breakthrough time of 50, which is much longer than that of $[\text{HO}]_{100\%}\text{-H}_2\text{P-COF}$ (15). Figure 3d compares the breakthrough characteristics of COFs in terms of mol % CO_2 at the outlet as a function of dimensionless time for operation at a total pressure of 100 kPa. $[\text{HO}]_{100\%}\text{-H}_2\text{P-COF}$ (red curve) has a breakthrough time much longer than that of $[\text{HO}]_{100\%}\text{-H}_2\text{P-COF}$ (blue curve). Longer breakthrough times are desirable for greater CO_2 capture. For a quantitative evaluation of the COFs, we arbitrarily chose the required outlet gas purity to be < 0.05 mol % CO_2 . Using this purity specification, we determined the breakthrough times, τ_{break} , for each COF. On the basis of the material balance on the adsorber, we determined the amount of CO_2 captured during the time interval $0\text{--}\tau_{\text{break}}$. Figure 3e presents a plot of the number of mmol of CO_2 captured per L of adsorbent during the time interval $0\text{--}\tau_{\text{break}}$ against the breakthrough time τ_{break} . Notably, $[\text{HO}_2\text{C}]_{100\%}\text{-H}_2\text{P-COF}$ (red circle) exhibited superior CO_2 productivity compared with $[\text{HO}]_{100\%}\text{-H}_2\text{P-COF}$ (black circle).

The aforementioned results indicate that channel-wall functionalization is efficient to convert a conventional COF into outstanding CO_2 adsorption materials; the effects of functional groups on carbon dioxide capture are positive and profound ranging from capacity to selectivity and productivity. To examine the cycle performance of $[\text{HO}_2\text{C}]_{100\%}\text{-H}_2\text{P-COF}$ in terms of CO_2 uptake, we conducted temperature and vacuum swings with a Belsorp mini II analyzer by saturating the samples with CO_2 up to 1.0 bar at 273 K followed by placing the samples under high vacuum for 60 min at 353 K. Remarkably, after ten cycles, no significant decline in uptake capacity was observed (Figure 3f), indicating complete desorption in each regeneration cycle and excellent cycling performance. These features assure a green process in regenerating the adsorbents.

In summary, we developed a strategy for converting a conventional 2D COF into an outstanding CO_2 capture scaffold through channel-wall functionalization. The high-throughput ring opening reaction is useful for creating carboxylic-acid-functionalized channel walls while retaining the layered and open porous structure. Given the rather limited room for increasing the porosity of 2D COFs, together with the availability of a broad diversity of different functional groups, we anticipate that the present channel-wall engineering strategy will be critical to exploring 2D COFs for high-performance gas storage and separation.

Received: November 20, 2014

Revised: December 26, 2014

Published online: January 22, 2015

Keywords: carbon dioxide · covalent organic frameworks · flue gas separation · gas adsorption · synthesis

- [1] a) X. Feng, X. S. Ding, D. Jiang, *Chem. Soc. Rev.* **2012**, *41*, 6010–6022; b) M. Dogru, T. Bein, *Chem. Commun.* **2014**, *50*, 5531–5546.
- [2] a) X. Feng, L. Liu, Y. Honsho, A. Saeki, S. Seki, S. Irle, Y. Dong, A. Nagai, D. Jiang, *Angew. Chem. Int. Ed.* **2012**, *51*, 2618–2622; *Angew. Chem.* **2012**, *124*, 2672–2676; b) Z. Li, X. Feng, Y. Zou, Y. Zhang, H. Xia, X. Liu, Y. Mu, *Chem. Commun.* **2014**, *50*, 13825–13828; c) A. Nagai, Z. Guo, X. Feng, S. Jin, X. Chen, X. Ding, D. Jiang, *Nat. Commun.* **2011**, *2*, 536; d) H. Xu, X. Chen, J. Gao, J. Lin, M. Addicoat, S. Irle, D. Jiang, *Chem. Commun.* **2014**, *50*, 1292–1294.
- [3] a) L. Stegbauer, K. Schwinghammer, B. V. Lotsch, *Chem. Sci.* **2014**, *5*, 2789–2793; b) S. Kandambeth, D. B. Shinde, M. K. Panda, B. Lukose, T. Heine, R. Banerjee, *Angew. Chem. Int. Ed.* **2013**, *52*, 13052–13056; *Angew. Chem.* **2013**, *125*, 13290–13294; c) H. Furukawa, O. M. Yaghi, *J. Am. Chem. Soc.* **2009**, *131*, 8875–8883; d) C. J. Doonan, D. J. Tranchemontagne, T. G. Glover, J. R. Hunt, O. M. Yaghi, *Nat. Chem.* **2010**, *2*, 235–238; e) S. Chandra, S. Kandambeth, B. P. Biswal, B. Lukose, S. M. Kunjir, M. Chaudhary, R. Babarao, T. Heine, R. Banerjee, *J. Am. Chem. Soc.* **2013**, *135*, 17853–17861.
- [4] a) Q. Fang, Z. Zhuang, S. Gu, R. B. Kaspar, J. Zheng, J. Wang, S. Qiu, Y. Yan, *Nat. Commun.* **2014**, *5*, 4503; b) D. N. Bunck, W. R. Dichtel, *Angew. Chem. Int. Ed.* **2012**, *51*, 1885–1889; *Angew. Chem.* **2012**, *124*, 1921–1925; c) D. N. Bunck, W. R. Dichtel, *Chem. Commun.* **2013**, *49*, 2457–2459.
- [5] a) Z. Kahveci, T. Islamoglu, G. A. Shar, R. Ding, H. M. El-Kaderi, *CrystEngComm* **2013**, *15*, 1524–1527; b) M. G. Rabbani, A. K. Sekizkardes, Z. Kahveci, T. E. Reich, R. Ding, H. M. El-Kaderi, *Chem. Eur. J.* **2013**, *19*, 3324–3328.
- [6] a) R. Dawson, D. J. Adams, A. I. Cooper, *Chem. Sci.* **2011**, *2*, 1173–1177; b) G. T. Rochelle, *Science* **2009**, *325*, 1652–1654; c) A. Torrisi, R. G. Bell, C. Mellot-Draznieks, *Cryst. Growth Des.* **2010**, *10*, 2839–2841; d) N. Hiyoshi, K. Yogo, T. Yashima, *Microporous Mesoporous Mater.* **2005**, *84*, 357–365; e) J. C. Hicks, J. H. Drese, D. J. Fauth, M. L. Gray, G. Qi, C. W. Jones, *J. Am. Chem. Soc.* **2008**, *130*, 2902–2903; f) T. Gadzikwa, O. K. Farha, K. L. Mulfort, J. T. Hupp, S. T. Nguyen, *Chem. Commun.* **2009**, 3720–3722; g) W. Lu, D. Yuan, J. Sculley, D. Zhao, R. Krishna, H. C. Zhou, *J. Am. Chem. Soc.* **2011**, *133*, 18126–18129; h) L. Wang, R. T. Yang, *J. Phys. Chem. C* **2012**, *116*, 1099–1106; i) W. Lu, J. P. Sculley, D. Yuan, R. Krishna, Z. Wei, H. C. Zhou, *Angew. Chem. Int. Ed.* **2012**, *51*, 7480–7484; *Angew. Chem.* **2012**, *124*, 7598–7602; j) P. Chowdhury, S. Mekala, F. Dreisbach, S. Gumma, *Microporous Mesoporous Mater.* **2012**, *152*, 246–252; k) P. D. C. Dietzel, V. Besikiotis, R. Blom, *J. Mater. Chem.* **2009**, *19*, 7362–7370; l) J. A. Mason, K. Sumida, Z. R. Herm, R. Krishna, J. R. Long, *Energy Environ. Sci.* **2011**, *4*, 3030–3040; m) S. R. Caskey, A. G. Wong-Foy, A. J. Matzger, *J. Am. Chem. Soc.* **2008**, *130*, 10870–10871; n) Y. Belmabkhout, G. Pirngruber, E. Jolimaite, A. Methivier, *Adsorption* **2007**, *13*, 341–349; o) S. Cavenati, C. A. Grande, A. E. Rodrigues, *J. Chem. Eng. Data* **2004**, *49*, 1095–1101; p) H. Jiang, D. Feng, T. Liu, J. Li, H. Zhou, *J. Am. Chem. Soc.* **2012**, *134*, 14690–14693; q) Y. Zhu, W. Zhang, *Chem. Sci.* **2014**, *5*, 4957–4961.
- [7] a) A. L. Myers, J. M. Prausnitz, *AIChE J.* **1965**, *11*, 121–127; b) R. Krishna, J. R. Long, *J. Phys. Chem. C* **2011**, *115*, 12941–12950.

Supporting Information

© Wiley-VCH 2015

69451 Weinheim, Germany

Two-Dimensional Covalent Organic Frameworks for Carbon Dioxide Capture through Channel-Wall Functionalization

*Ning Huang, Xiong Chen, Rajamani Krishna, and Donglin Jiang**

anie_201411262_sm_miscellaneous_information.pdf

Contents

Section A. Methods

Section B. Materials and synthetic procedures

Section C. Fitting of pure component isotherms

Section D. Isostatic heat of adsorption

Section E. IAST calculations

Section F. Simulation methodology for breakthrough in fixed bed absorbers

Section G. Notation

Section H. Supporting tables

Section I. Supporting figures

Section J. Supporting references

Section A. Methods

Fourier transform Infrared (FT IR) spectra were recorded on a JASCO model FT IR-6100 infrared spectrometer. UV-Vis-IR diffuse reflectance spectrum (Kubelka-Munk spectrum) was recorded on a JASCO model V-670 spectrometer equipped with integration sphere model IJN-727. Powder X-ray diffraction (PXRD) data were recorded on a Rigaku model RINT Ultima III diffractometer by depositing powder on glass substrate, from $2\theta = 1.5^\circ$ up to 60° with 0.02° increment. Elemental analysis was performed on a Yanako CHN CORDER MT-6 elemental analyzer. TGA measurements were performed on a Mettler-Toledo model TGA/SDTA851^o under N₂, by heating to 800 °C at a rate of 10 °C min⁻¹. Nitrogen sorption isotherms were measured at 77 K with a Bel Japan Inc. model BELSORP-mini II analyzer. Before measurement, the samples were degassed in vacuum at 120 °C for more than 10 h. By using the non-local density functional theory (NLDFT) model, the pore volume was derived from the sorption curve. ¹H NMR spectra were recorded on a JEOL model JNM-LA400 NMR spectrometer, where the chemical shifts (δ in ppm) were determined with a residual proton of the solvent as standard. Scanning electron microscopy (SEM) was carried out using solid samples on Hitachi Hitechnology C C model SU6600 and energy dispersive X-ray spectrometry (EDX) was recorded on Bruker AXS model using Quantax system with XFlash 6|10 detector.

Section B. Materials and synthetic procedures

1-Butanol, *o*-dichlorobenzene (*o*-DCB), anhydrous acetone (99.5%), tetrahydrofuran, and acetic acid were purchased from Wako Chemicals. succinic anhydride and 1,4-phthalaldehyde (PA) was purchased from TCI. Free-base 5,10,15,20-tetrakis(*p*-tetraphenylamino) porphyrin (H₂P) was prepared from *p*-nitrobenzaldehyde using a literature procedure.^{S1}

2,5-Dihydroxyterephthalaldehyde (DHTA) was synthesized according to a reported method.^{S2}

[HO]_{x%}-H₂P-COFs. An *o*-DCB/BuOH/6 M AcOH mixture (5/5/1 by vol.; 1.1 mL) of H₂P (0.02 mmol, 13.48 mg) and DHTA/PA (total 0.04 mmol) at different molar ratios of 25/75, 50/50, 75/25, and 100/0 was degassed in a Pyrex tube (10 mL) by three freeze-pump-thaw cycles. The tube was sealed off and heated at 120 °C for three days. The precipitate was collected by centrifugation, washed with anhydrous THF for five times, and washed with acetone twice. The powder was dried at 120 °C under vacuum overnight to give the corresponding product in isolated yields of 78%, 75%, 84%, and 82% for [HO]_{25%}-H₂P-COF, [HO]_{50%}-H₂P-COF, [HO]_{75%}-H₂P-COF, and [HO]_{100%}-H₂P-COF, respectively.

[HO₂C]_{x%}-H₂P-COFs. [HO]_{x%}-H₂P-COFs (30 mg) was weighed into a 10-mL glass vial, to which succinic anhydride (6 mL, 1.0 M solution in anhydrous acetone) was added. The reaction mixture was heated at 60 °C for two days. The precipitate was collected by centrifugation, washed with anhydrous THF for five times. The crude product was rinsed with THF for 48 h using a Soxhlet extractor. The powder was dried at 100 °C under vacuum overnight to give the corresponding products of [HO₂C]_{25%}-H₂P-COF, [HO₂C]_{50%}-H₂P-COF, [HO₂C]_{75%}-H₂P-COF, and [HO₂C]_{100%}-H₂P-COF, quantitatively.

Hydrolysis of [HO₂C]_{x%}-H₂P-COFs. The [HO₂C]_{x%}-H₂P-COFs (100 mg) sample were hydrolyzed by refluxing in a THF/H₂O (2/1 by vol., 24 mL) solution of KOH (3 M) for 5 days. After filtration, 5 mL of aqueous HCl solution (6 M) was added slowly to the filtrate and the mixture was stirred for 1 h. The greenish porphyrin precipitate was removed by filtration. The filtrate was evaporated under vacuum and submitted to ¹H NMR spectroscopy in *d*₆-DMSO. The content of carboxylic acid was calculated by using the proton integrates (Table S3, Figure S5).

Section C. Fitting of pure component isotherms

The salient properties of two different COFs ([HO]_{100%}-H₂P-COF and [HO₂C]_{100%}-H₂P-COF) are specified in Table 1. The potential of these COFs are evaluated for the separation of CO₂/N₂ mixtures that is relevant for CO₂ capture from flue gases. For our evaluations, we assume the CO₂/N₂ mixtures to contain 15% CO₂, and 85% N₂, following the earlier work of Mason et al.^{S1}

The experimentally measured excess loadings of CO₂, and N₂, obtained at different temperatures, were first converted to absolute loadings before data fitting. The procedure for converting to absolute loadings is the same as described in the Supporting Information accompanying the paper of Wu et al.^{S2} For the purpose of converting to absolute loadings, the pore volumes used are specified in Table S4. The isotherm data for CO₂ were fitted with the Langmuir-Freundlich model:

$$q = q_{sat} \frac{bp^v}{1 + bp^v} \quad (1)$$

with T -dependent parameter b

$$b_A = b_0 \exp\left(\frac{E}{RT}\right) \quad (2)$$

The Langmuir-Freundlich parameters for adsorption of CO₂ are provided in Table S5. The simpler Langmuir model was adequate for fitting the isotherm data for N₂; Table S6 provides the T -dependent Langmuir parameters for N₂ in different materials.

Section D. Isotheric heat of adsorption

The isosteric heat of adsorption, Q_{st} , defined as

$$Q_{st} = RT^2 \left(\frac{\partial \ln p}{\partial T} \right)_q \quad (3)$$

was determined using the pure component isotherm fits using the Clausius-Clapeyron equation.

Section E. IAST calculations

The selectivity of preferential adsorption of component 1 over component 2 in a mixture containing 1 and 2, perhaps in the presence of other components too, can be formally defined as

$$S_{ads} = \frac{q_1/q_2}{P_1/P_2} \quad (4)$$

In equation (4), q_1 and q_2 are the *absolute* component loadings of the adsorbed phase in the mixture. These component loadings are also termed the uptake capacities. In all the calculations to be presented below, the calculations of q_1 and q_2 are based on the use of the Ideal Adsorbed Solution Theory (IAST) of Myers and Prausnitz.^{S3} The accuracy of the IAST calculations for estimation of the component loadings for several binary mixtures in a wide variety of zeolites, and MOFs has been established by comparison with Configurational-Bias Monte Carlo (CBMC) simulations of mixture adsorption.^{S4-S9}

Section F. Simulation methodology for transient breakthrough in fixed bed absorbers

The separation of CO₂/N₂ mixtures is commonly carried out in fixed bed absorbers in which the separation performance is dictated by a combination of three separate factors: (a) adsorption selectivity, (b) uptake capacity, and (c) intra-crystalline diffusivities of guest molecules within the pores. Transient breakthrough simulations are required for a proper evaluation of MOFs; the simulation methodology used in our work is described in earlier publications.^{S10,S11} A brief summary of the simulation methodology is presented below.

Assuming plug flow of an n -component gas mixture through a fixed bed maintained under isothermal conditions (see schematic in Figure 4a), the partial pressures in the gas phase at any position and instant of time are obtained by solving the following set of partial differential equations for each of the species i in the gas mixture.^{S12}

$$\frac{1}{RT} \frac{\partial p_i(t, z)}{\partial t} = -\frac{1}{RT} \frac{\partial (v(t, z) p_i(t, z))}{\partial z} - \frac{(1 - \varepsilon)}{\varepsilon} \rho \frac{\partial \bar{q}_i(t, z)}{\partial t}; \quad i = 1, 2, \dots, n \quad (5)$$

In equation (5), t is the time, z is the distance along the adsorber, r is the framework density, ε is the bed voidage, v is the interstitial gas velocity, and $\bar{q}_i(t, z)$ is the *spatially averaged* molar loading within the crystallites of radius r_c , monitored at position z , and at time t .

At any time t , during the transient approach to thermodynamic equilibrium, the spatially averaged molar loading within the crystallite r_c is obtained by integration of the radial loading profile

$$\bar{q}_i(t) = \frac{3}{r_c^3} \int_0^{r_c} q_i(r, t) r^2 dr \quad (6)$$

For transient unary uptake within a crystal at any position and time with the fixed bed, the radial distribution of molar loadings, q_i , within a spherical crystallite, of radius r_c , is obtained from a solution of a set of differential equations describing the uptake

$$\frac{\partial q_i(r, t)}{\partial t} = -\frac{1}{\rho} \frac{1}{r^2} \frac{\partial}{\partial r} (r^2 N_i) \quad (7)$$

The molar flux N_i of component i is described by the simplified version of the Maxwell-Stefan equations in which both correlation effects and thermodynamic coupling effects are considered to be of negligible importance¹²

$$N_i = -\rho D_i \frac{\partial q_i}{\partial r} \quad (8)$$

Summing equation (6) over all n species in the mixture allows calculation of the *total average* molar loading of the mixture within the crystallite

$$\bar{q}_i(t, z) = \sum_{i=1}^n \bar{q}_i(t, z) \quad (9)$$

The *interstitial* gas velocity is related to the *superficial* gas velocity by

$$v = \frac{u}{\varepsilon} \quad (10)$$

In industrial practice, the most common operation uses a step-wise input of mixtures to be separated into an absorber bed that is initially free of adsorbents, i.e. we have the initial condition

$$t = 0; \quad q_i(0, z) = 0 \quad (11)$$

At time $t = 0$, the inlet to the absorber, $z = 0$, is subjected to a step input of the n -component gas mixture and this step input is maintained till the end of the adsorption cycle when steady-state conditions are reached.

$$t \geq 0; \quad p_i(0, t) = p_{i0}; \quad u(0, t) = u_0 \quad (12)$$

where u_0 is the superficial gas velocity at the inlet to the absorber.

The breakthrough characteristics for any component is essentially dictated by two sets of parameters: (a) The characteristic contact time $\frac{L}{v} = \frac{L\varepsilon}{u}$ between the crystallites and the surrounding fluid phase, and (b) $\frac{D_i}{r_c^2}$, that reflect the importance of intra-crystalline diffusion limitations. It is common to use the dimensionless time, $\tau = \frac{tu}{L\varepsilon}$, obtained by dividing the actual time t , by the characteristic time, $\frac{L\varepsilon}{u}$ when plotting simulated breakthrough curves.¹¹

If the value of $\frac{D_i}{r_c^2}$ is large enough to ensure that intra-crystalline gradients are absent and the entire crystallite particle can be considered to be in thermodynamic equilibrium with the surrounding bulk gas phase at that time t , and position z of the adsorber

$$\bar{q}_i(t, z) = q_i(t, z) \quad (13)$$

The molar loadings at the *outer surface* of the crystallites, i.e. at $r = r_c$, are calculated on the basis of adsorption equilibrium with the bulk gas phase partial pressures p_i at that position z and time t . The adsorption equilibrium can be calculated on the basis of the IAST. The assumption of

thermodynamic equilibrium at every position z , and any time t , i.e. invoking Equation (13), generally results in sharp breakthroughs for each component. Sharp breakthroughs are desirable in practice because this would result in high productivity of pure products. Essentially, the influence of intra-crystalline diffusion is to reduce the productivity of pure gases. For all the breakthrough calculations reported in this work, we assume negligible diffusion resistances for all materials and we invoke the simplified Equation (13).

Section G. Notation

b_A	dual-Langmuir-Freundlich constant for species i at adsorption site A, $\text{Pa}^{-\nu_i}$
c_i	molar concentration of species i in gas mixture, mol m^{-3}
c_{i0}	molar concentration of species i in gas mixture at inlet to adsorber, mol m^{-3}
L	length of packed bed adsorber, m
N	number of species in the mixture, dimensionless
N_i	molar flux of species i , $\text{mol m}^{-2} \text{s}^{-1}$
p_i	partial pressure of species i in mixture, Pa
p_t	total system pressure, Pa
q_i	component molar loading of species i , mol kg^{-1}
$\bar{q}_i(t)$	<i>spatially averaged</i> component molar loading of species i , mol kg^{-1}
r_c	radius of crystallite, m
R	gas constant, $8.314 \text{ J mol}^{-1} \text{ K}^{-1}$
t	time, s
T	absolute temperature, K
u	superficial gas velocity in packed bed, m s^{-1}
v	interstitial gas velocity in packed bed, m s^{-1}

Greek letters

e	voidage of packed bed, dimensionless
r	framework density, kg m^{-3}
τ	time, dimensionless

Subscripts

i	referring to component
i_{break}	referring to breakthrough
t	referring to total mixture

Section H. Supporting tables

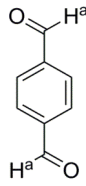
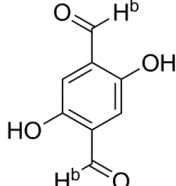
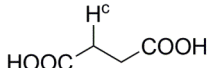
Table S1. Elemental analysis results of [HO]_x-H₂P-COFs and [HO₂C]_x-H₂P-COFs

COFs		C%	H%	N%
[HO] _{100%} -H ₂ P-COF	Calcd.	76.95	4.25	11.97
	Found	74.92	4.88	10.87
[HO] _{75%} -H ₂ P-COF	Calcd.	78.29	4.33	12.17
	Found	76.68	4.68	11.54
[HO] _{50%} -H ₂ P-COF	Calcd.	79.67	4.40	12.39
	Found	78.24	4.87	10.92
[HO] _{25%} -H ₂ P-COF	Calcd.	81.11	4.48	12.61
	Found	78.62	5.03	11.28
[HO ₂ C] _{25%} -H ₂ P-COF	Calcd.	74.05	4.37	10.79
	Found	70.42	4.87	8.67
[HO ₂ C] _{50%} -H ₂ P-COF	Calcd.	71.76	4.34	9.85
	Found	69.34	4.71	8.72
[HO ₂ C] _{75%} -H ₂ P-COF	Calcd.	69.84	4.31	9.05
	Found	68.46	4.92	7.82
[HO ₂ C] _{100%} -H ₂ P-COF	Calcd.	68.21	4.29	8.37
	Found	64.43	5.17	7.02

Table S2. Energy dispersive X-ray spectrometry (EDX) analysis of [HO]_x%-H₂P-COFs and [HO₂C]_x%-H₂P-COFs

COFs		C%	O%	N%
[HO] ₁₀₀ %-H ₂ P-COF	Calcd.	76.95	6.83	11.97
	Found	77.36	5.92	12.50
[HO] ₇₅ %-H ₂ P-COF	Calcd.	78.29	5.21	12.17
	Found	77.2	5.01	13.41
[HO] ₅₀ %-H ₂ P-COF	Calcd.	79.67	3.54	12.39
	Found	78.8	3.83	12.91
[HO] ₂₅ %-H ₂ P-COF	Calcd.	81.11	1.8	12.61
	Found	82.93	1.81	10.92
[HO ₂ C] ₂₅ %-H ₂ P-COF	Calcd.	74.05	10.79	10.79
	Found	74.50	10.06	11.06
[HO ₂ C] ₅₀ %-H ₂ P-COF	Calcd.	71.76	14.05	9.85
	Found	70.33	14.95	10.38
[HO ₂ C] ₇₅ %-H ₂ P-COF	Calcd.	69.84	16.8	9.05
	Found	68.61	16.98	10.09
[HO ₂ C] ₁₀₀ %-H ₂ P-COF	Calcd.	68.21	19.13	8.37
	Found	67.08	19.70	8.92

Table S3. Analysis of proton integration of hydrolyzed samples of [HO₂C]_x%-H₂P-COFs

COFs	Fragment after hydrolysis	PA 10.25 ppm	DHTA 10.01 ppm	Succinic Acid 2.45 ppm
	structure			
[HO ₂ C] ₂₅ %-H ₂ P-COF	Proton Integration	6.84	2	9.02
	Content of carboxylic acid ^a	$= 9.02/4(6.84 + 2) \times 100\% = 25.5\%$		
[HO ₂ C] ₅₀ %-H ₂ P-COF	Proton Integration	4.55	4	17.76
	Content of carboxylic acid	$= 17.76/4(4.55 + 4) \times 100\% = 51.9\%$		
[HO ₂ C] ₇₅ %-H ₂ P-COF	Proton Integration	2.58	6	26.43
	Content of carboxylic acid	$= 26.43/4(6 + 2.58) \times 100\% = 77.1\%$		
[HO ₂ C] ₁₀₀ %-H ₂ P-COF	Proton Integration	0	8	33.20
	Content of carboxylic acid	$= 33.20/4(8 + 0) \times 100\% = 103\%$		

^aThe content of carboxylic acid was calculated by using the equation of $H^c/4(H^a + H^b) \times 100\%$.

The experimentally determined content of carboxylic acid was 25.5%, 51.9%, 77.1%, and 103%, which is consistent with the value of 25%, 50%, 75%, and 100%, calculated from the loading monomer ratios for [HO₂C]₂₅%-H₂P-COF, [HO₂C]₅₀%-H₂P-COF, [HO₂C]₇₅%-H₂P-COF, and [HO₂C]₁₀₀%-H₂P-COF, respectively.

Table S4. Salient properties of [HO]_{100%}-H₂P-COF and [HO₂C]_{100%}-H₂P-COF (The crystal framework densities, required in the breakthrough simulations, are estimated as (bulk density)/(one-bed porosity) with the assumption that the bed porosity is 0.4.)

COFs	Bulk density (g cm ⁻³)	S_{BET} (m ² g ⁻¹)	Pore volume (cm ³ g ⁻¹)	Pore size (nm)
[HO] _{100%} -H ₂ P-COF	0.24	1186	0.78	2.54
[HO ₂ C] _{100%} -H ₂ P-COF	0.26	326	0.49	1.56

Table S5. Langmuir-Freundlich parameters for adsorption of CO₂ in COFs (The experimentally measured excess loadings were first converted to absolute loadings before data fitting.)

COFs	q_{sat} (mol kg ⁻¹)	b_0 (Pa ^{-v})	E (kJ mol ⁻¹)	n (dimensionless)
[HO] _{100%} -H ₂ P-COF	2.2	1.4×10^{-11}	34.6	0.9
[HO ₂ C] _{100%} -H ₂ P-COF	7.7	6.04×10^{-11}	33.5	0.77

Table S6. One-site Langmuir parameters for N₂ in different materials

COFs	$q_{\text{A,sat}}$ (mol kg ⁻¹)	b_{A0} (Pa ⁻¹)	E_{A} (kJ mol ⁻¹)
[HO] _{100%} -H ₂ P-COF	1.2	6.14×10^{-12}	30.7
[HO ₂ C] _{100%} -H ₂ P-COF	2	2.38×10^{-11}	23.9

Section I. Supporting figures

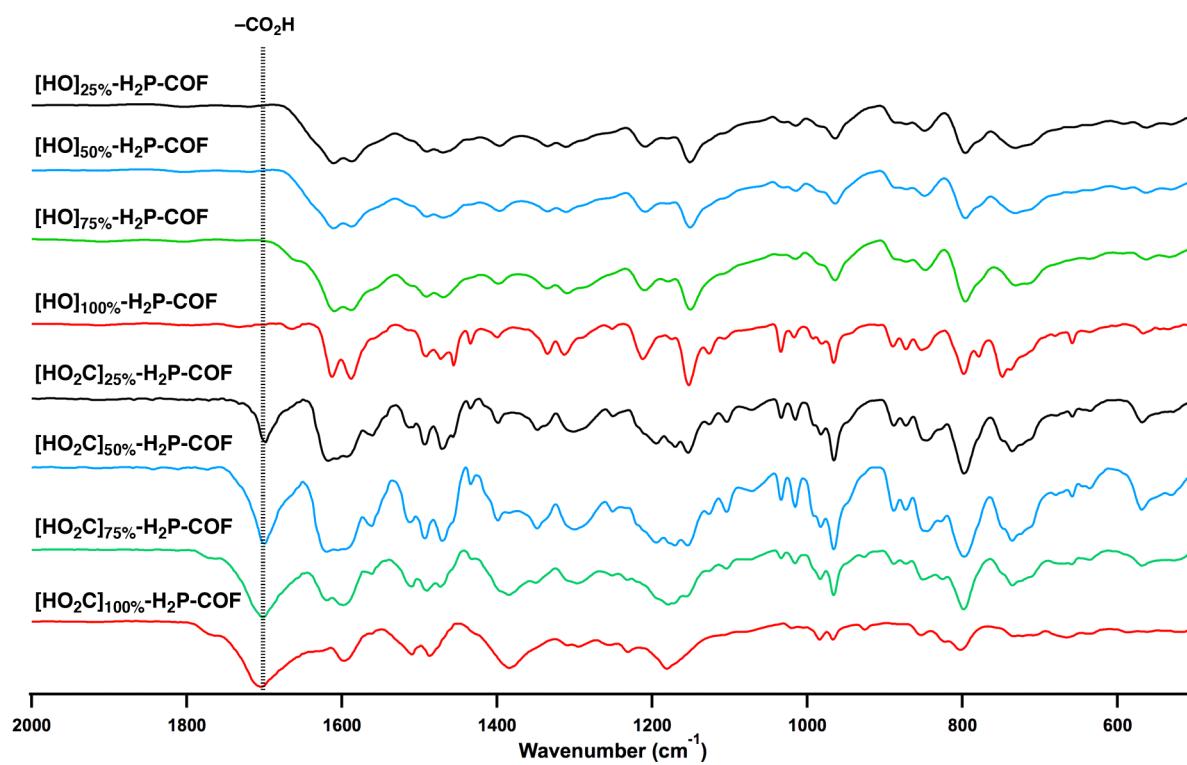


Figure S1. FT IR spectra of [HO]_{x%}-H₂P-COFs and [HO₂C]_{x%}-H₂P-COFs.

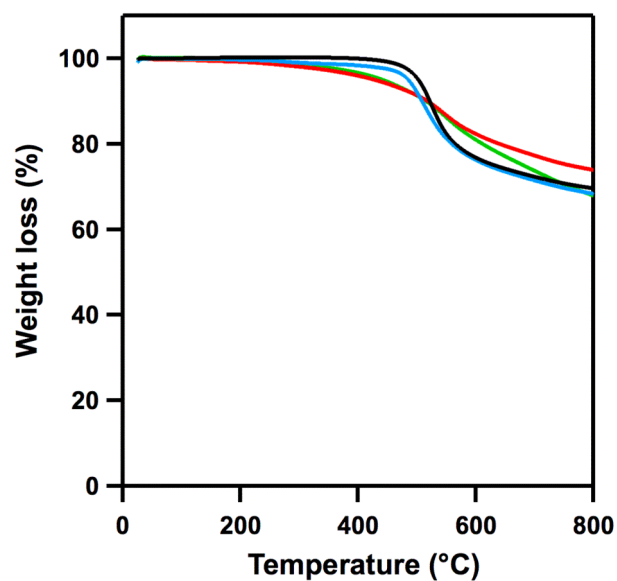


Figure S2. TGA curves of $[\text{HO}]_x\text{-H}_2\text{P-COFs}$ (red: $[\text{HO}]_{100\%}\text{-H}_2\text{P-COF}$, green: $[\text{HO}]_{75\%}\text{-H}_2\text{P-COF}$, blue: $[\text{HO}]_{50\%}\text{-H}_2\text{P-COF}$, black: $[\text{HO}]_{25\%}\text{-H}_2\text{P-COF}$).

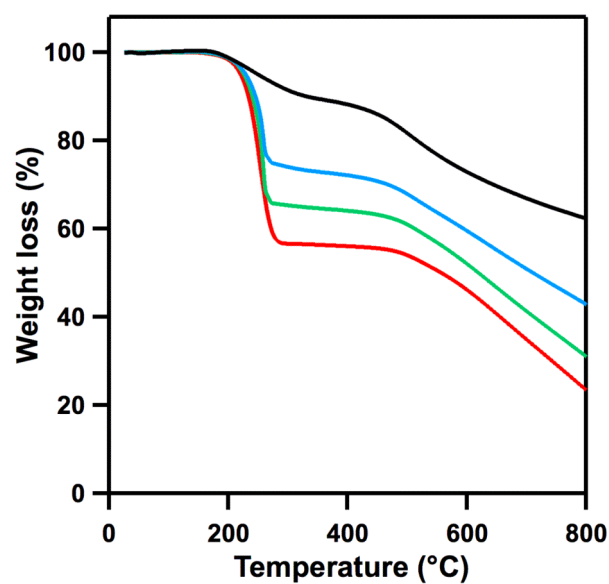


Figure S3. TGA curves of $[\text{HO}_2\text{C}]_x\text{-H}_2\text{P-COFs}$ (red: $[\text{HO}_2\text{C}]_{100\%}\text{-H}_2\text{P-COF}$, green: $[\text{HO}_2\text{C}]_{75\%}\text{-H}_2\text{P-COF}$, blue: $[\text{HO}_2\text{C}]_{50\%}\text{-H}_2\text{P-COF}$, black: $[\text{HO}_2\text{C}]_{25\%}\text{-H}_2\text{P-COF}$). The weight loss at 250 °C is due to the decomposition of linear chains on the channel walls and is consistent with the theoretical weight percentage of the chains in the COFs.

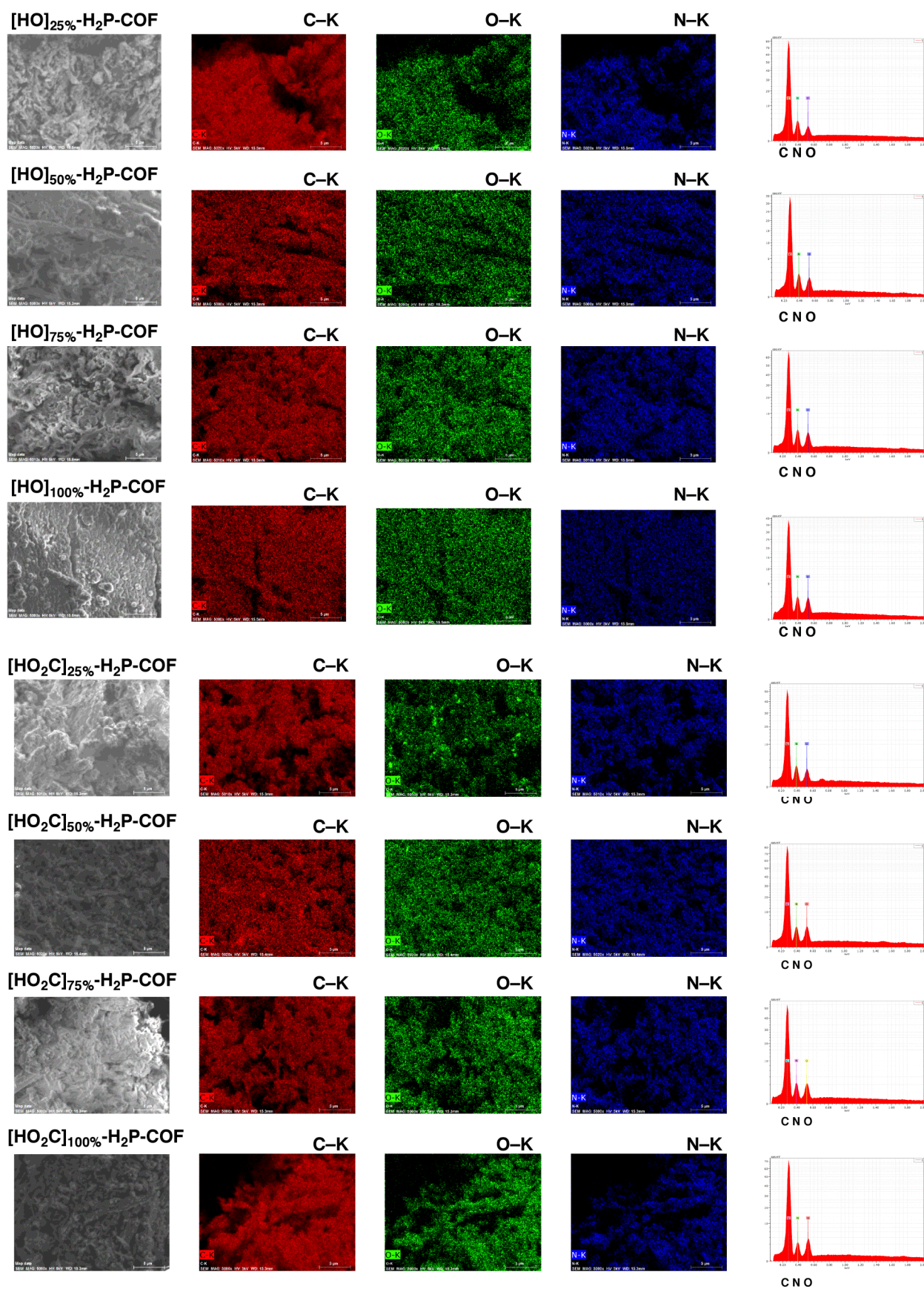


Figure S4. EDX analysis of [HO]_x%-H₂P-COFs and [HO₂C]_x%-H₂P-COFs.

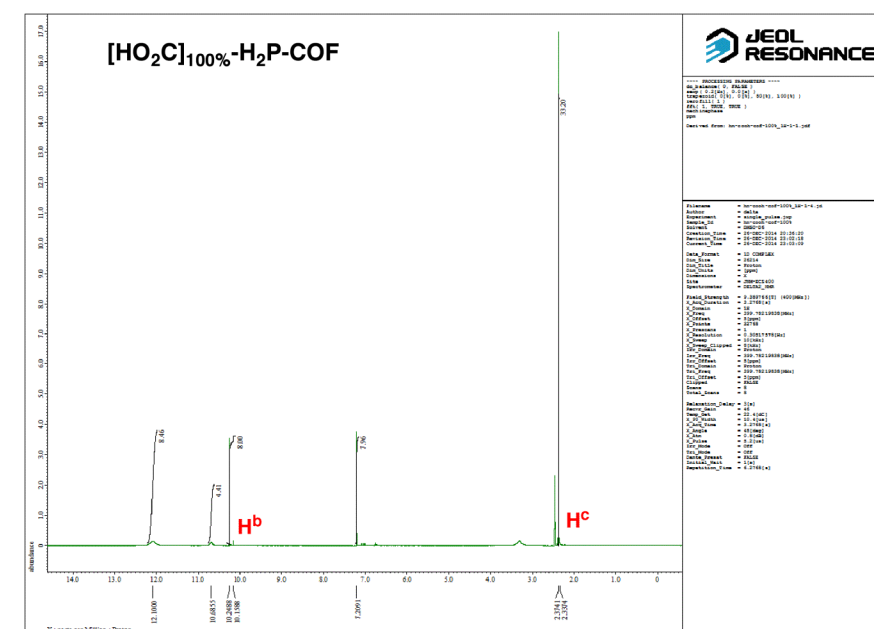
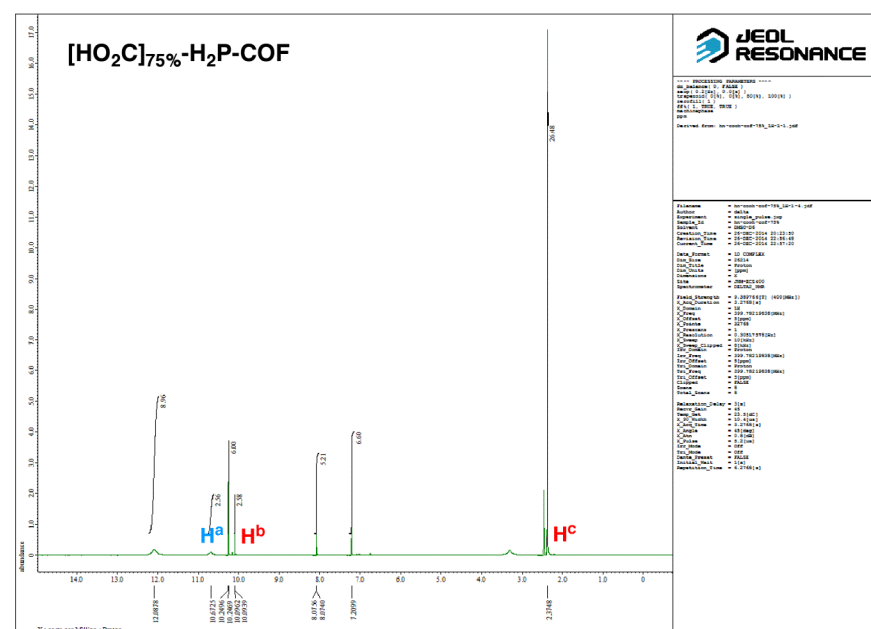
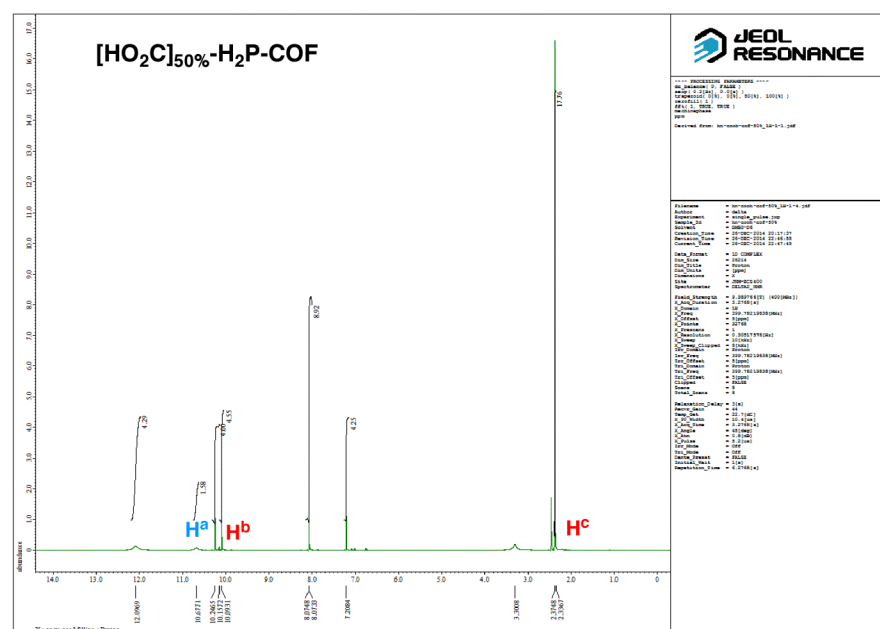
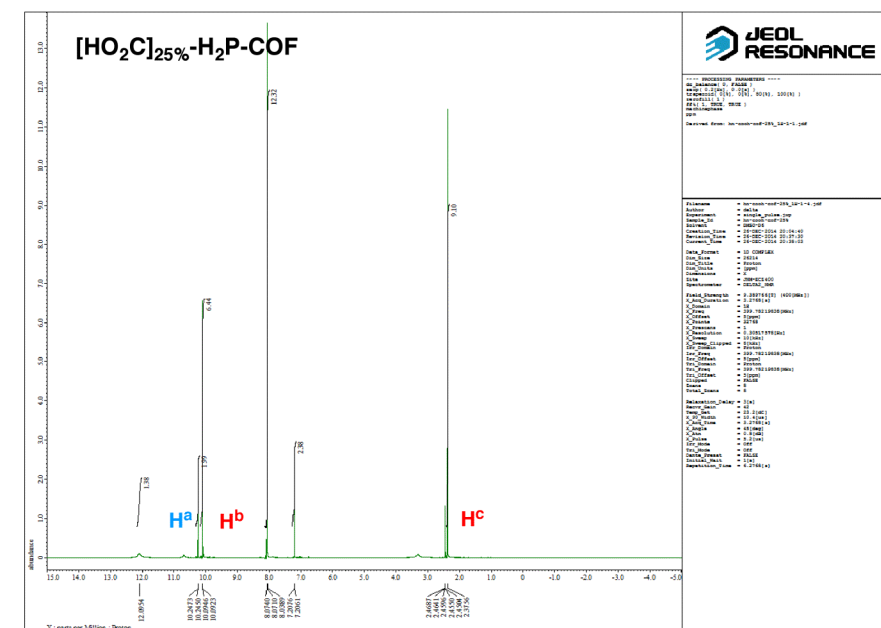
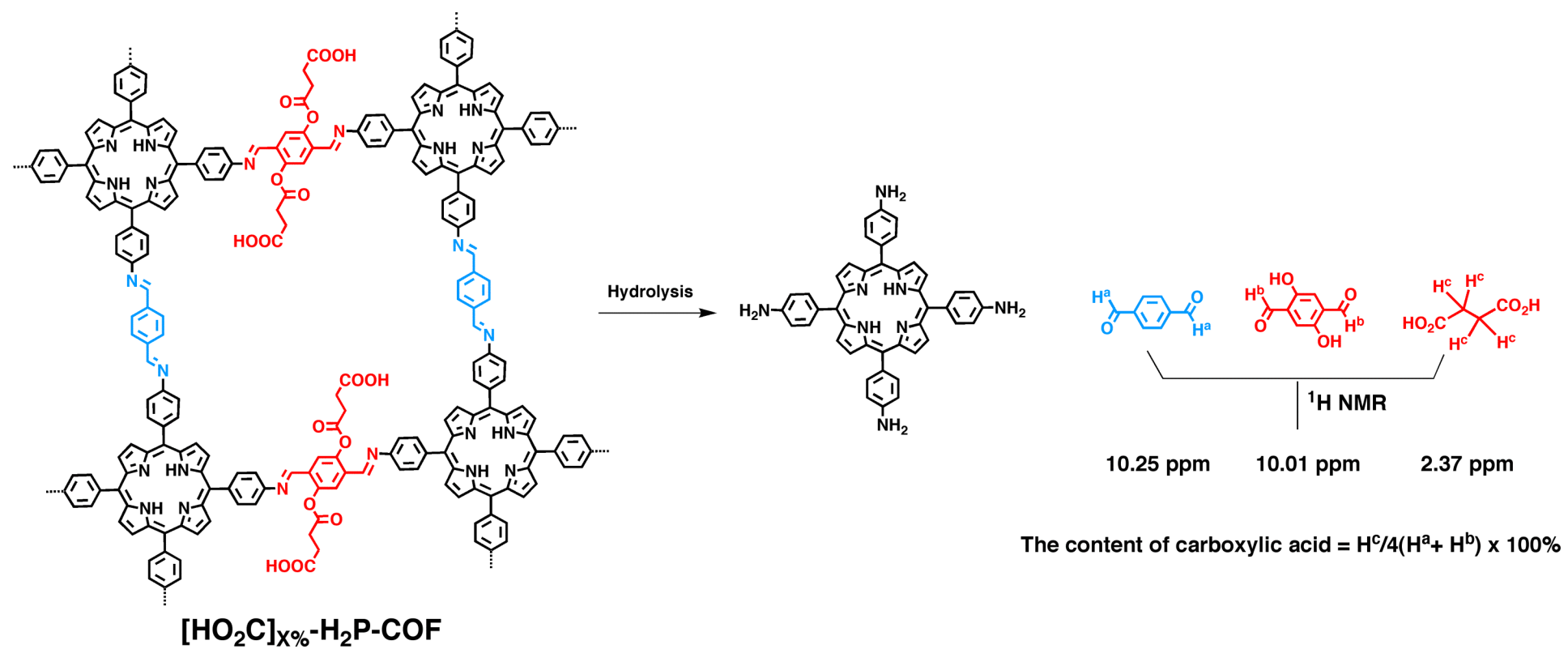


Figure S5. $^1\text{H NMR}$ spectra of hydrolyzed samples of $[\text{HO}_2\text{C}]_x\% \text{-H}_2\text{P-COF}$ s.

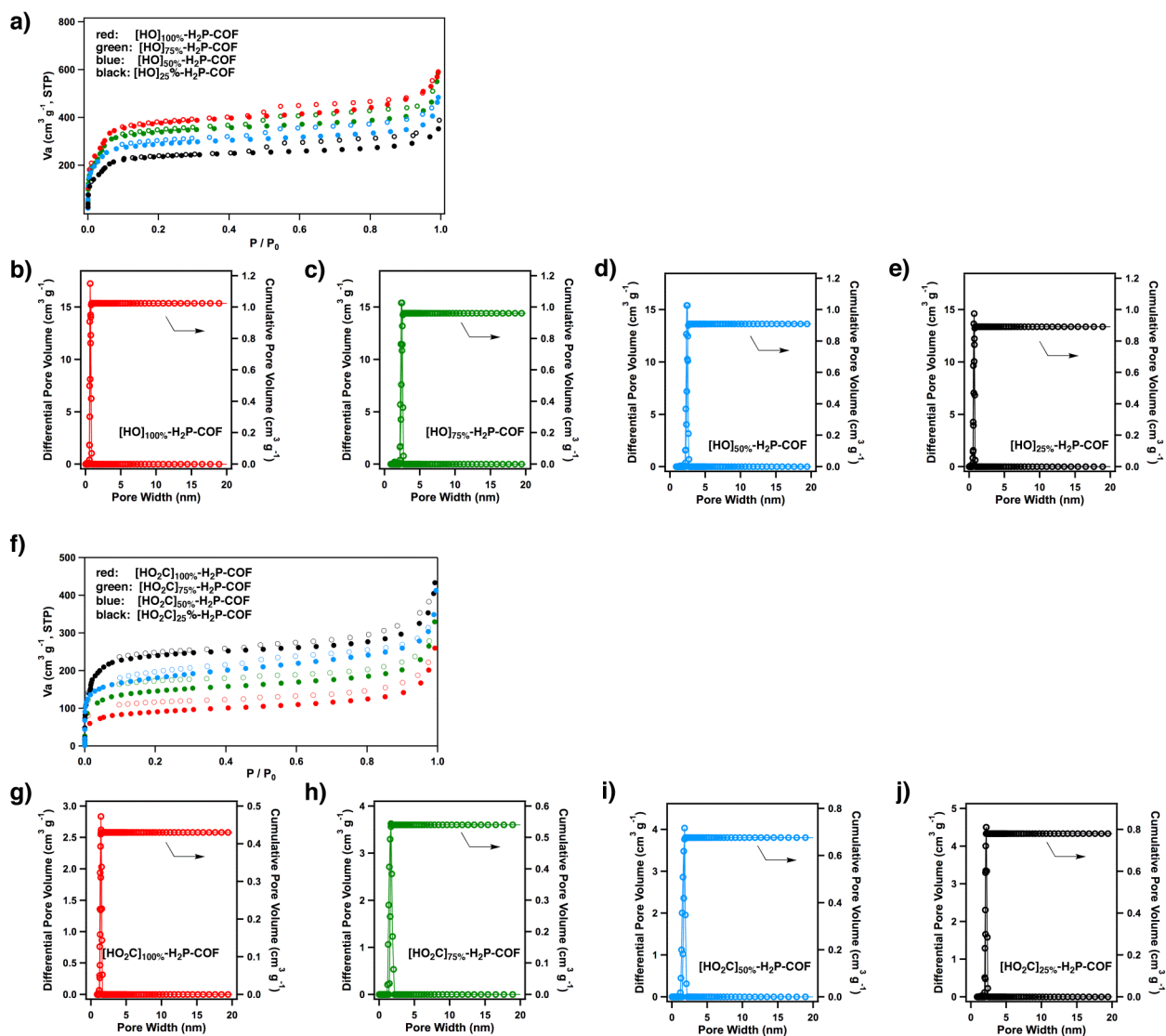


Figure S6. a) Nitrogen sorption isotherm curves of [HO]_x-H₂P-COFs. b-e) Pore size and pore size distribution profiles of [HO]_x-H₂P-COFs. f) Nitrogen sorption isotherm curves of [HO₂C]_x-H₂P-COFs. g-j) Pore size and pore size distribution profiles of [HO₂C]_x-H₂P-COFs.

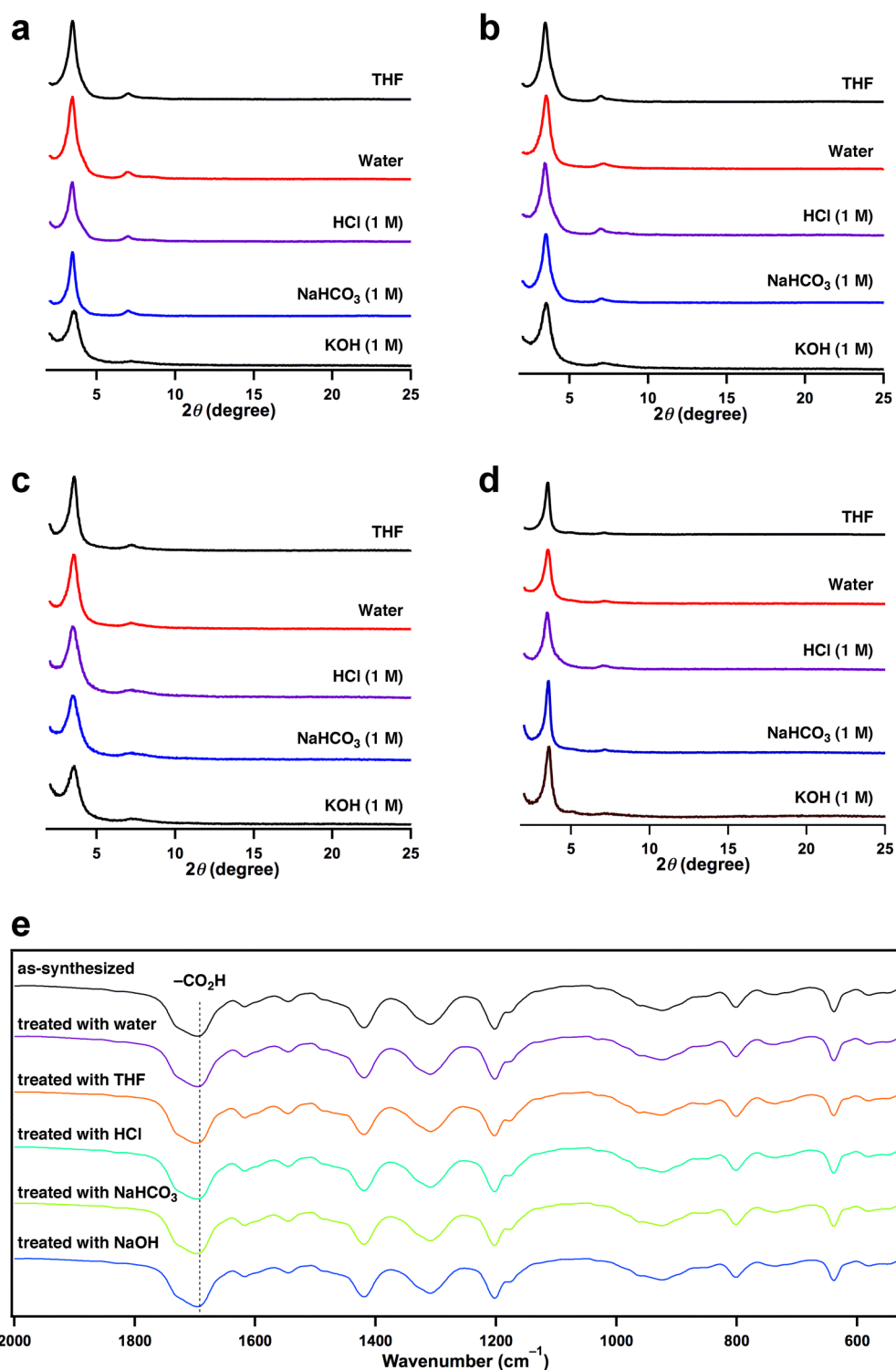


Figure S7. Stability test of [HO₂C]_x-H₂P-COFs. The XRD patterns of a) [HO₂C]_{25%}-H₂P-COF, b) [HO₂C]_{50%}-H₂P-COF, c) [HO₂C]_{75%}-H₂P-COF, and d) [HO₂C]_{100%}-H₂P-COF upon immersion in different solvents at room temperature for 24 h. (e) IR spectra of [HO₂C]_{100%}-H₂P-COF and the [HO₂C]_{100%}-H₂P-COF samples upon treatment with different solvents at room temperature for 24 h. These IR spectra revealed that the carboxylic acid groups were retained under these conditions.

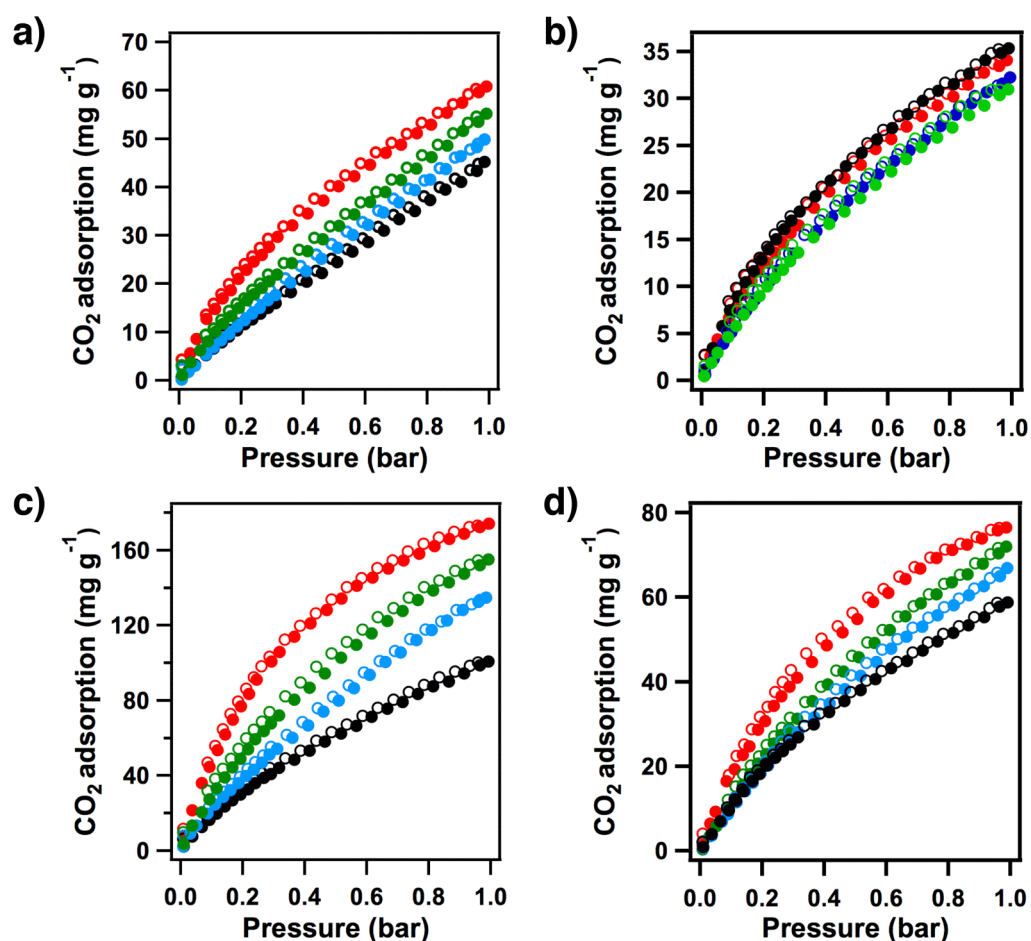


Figure S8. CO₂ sorption curves of [HO]_x%-H₂P-COFs measured at (a) 273 K and (b) 298 K (black: [HO]₂₅%-H₂P-COF, blue: [HO]₅₀%-H₂P-COF, green: [HO]₇₅%-H₂P-COF, red: [HO]₁₀₀%-H₂P-COF). CO₂ sorption curves of [HO₂C]_x%-H₂P-COFs measured at (c) 273 K and (d) 298 K (black: [HO₂C]₂₅%-H₂P-COF, blue: [HO₂C]₅₀%-H₂P-COF, green: [HO₂C]₇₅%-H₂P-COF, red: [HO₂C]₁₀₀%-H₂P-COF). Open and filled circles represent desorption and adsorption, respectively.

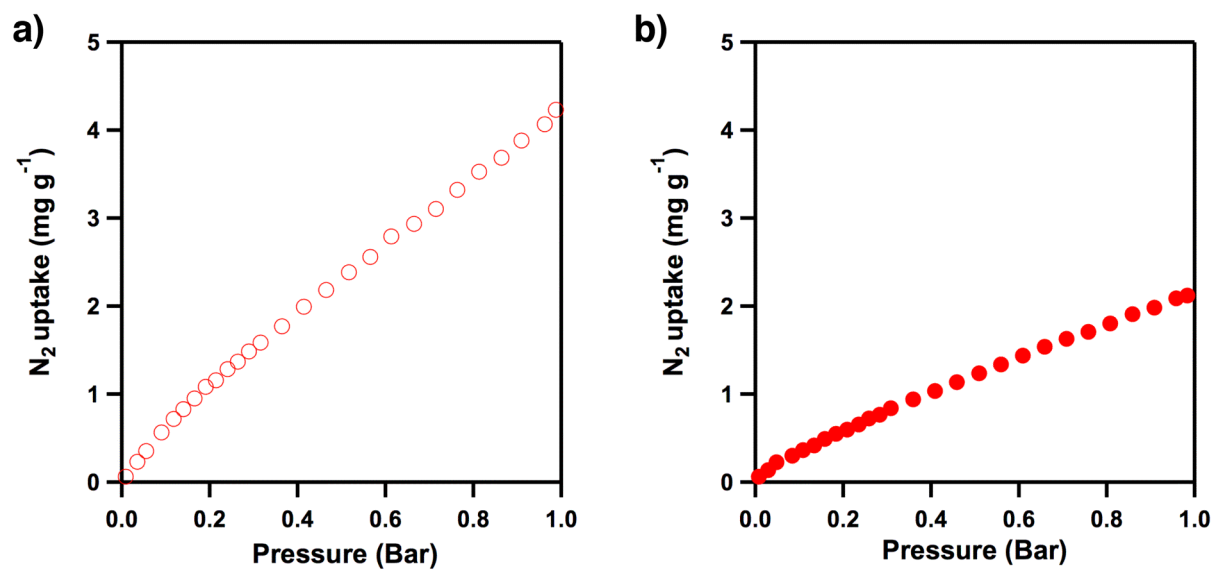


Figure S9. Nitrogen adsorption isotherm curves of a) [HO]_{100%}-H₂P-COF and b) [HO₂C]_{100%}-H₂P-COF measured at 298 K.

Section J. Supporting references

- S1. M. Yuasa, K. Oyaizu, A. Yamaguchi, M. Kuwakado *J. Am. Chem. Soc.* **2004**, *126*, 11128.
- S2. U. S. Hiremath, *Tetrahedron Letters* **2013**, *54*, 3419.
- S3. J. A. Mason, K. Sumida, Z. R. Herm, R. Krishna, J. R. Long, *Energy Environ. Sci.* **2011**, *4*, 3030.
- S4. H. Wu, K. Yao, Y. Zhu, B. Li, Z. Shi, R. Krishna, J. Li, *J. Phys. Chem. C* **2012**, *116*, 16609.
- S5. A. L. Myers, J. M. Prausnitz, *A.I.Ch.E.J.* **1965**, *11*, 121.
- S6. R. Krishna, J. M. van Baten, *Chem. Eng. J.* **2007**, *133*, 121.
- S7. R. Krishna, J. M. van Baten, *J. Membr. Sci.* **2010**, *360*, 323.
- S8. R. Krishna, J. M. van Baten, *Phys. Chem. Chem. Phys.* **2011**, *13*, 10593.
- S9. R. Krishna, J. M. van Baten, *J. Membr. Sci.* **2011**, *383*, 289.
- S10. R. Krishna, J. M. van Baten, *J. Membr. Sci.* **2011**, *377*, 249.
- S11. R. Krishna, J. M. van Baten, *Chem. Eng. Sci.* **2012**, *69*, 684.
- S12. R. Krishna, J. R. Long, *J. Phys. Chem. C* **2011**, *115*, 12941.
- S13. R. Krishna, *Microporous Mesoporous Mater.* **2014**, *185*, 30.
- S14. R. Krishna, R. Baur, *Sep. Purif. Technol.* **2003**, *33*, 213.